UC Santa Barbara
UC Santa Barbara Previously Published Works

Title

MnO Conversion in Li-Ion Batteries: In Situ Studies and the Role of Mesostructuring

Permalink

https://escholarship.org/uc/item/62v9t8q4

Journal

ACS Applied Materials & Interfaces, 8(10)

ISSN

1944-8244 1944-8252

Authors

Butala, Megan M
Danks, Katherine R
Lumley, Margaret A
et al.

Publication Date

2016-03-16

DOI

10.1021/acsami.5b12840

Peer reviewed

MnO Conversion in Li-Ion Batteries: In Situ Studies and the Role of Mesostructuring

Megan M. Butala,[*,†,‡] Katherine R. Danks,[†,∥] Margaret A. Lumley,[¶,‡]
Shiliang Zhou,[§] Brent C. Melot,[§] and Ram Seshadri[*,†,‡]

†*Materials Department and Materials Research Laboratory*
University of California, Santa Barbara, CA 93106
‡*Mitsubishi Chemical Center for Advanced Materials*
University of California, Santa Barbara, CA 93106
¶*Department of Chemistry and Biochemistry*
University of California, Santa Barbara, CA 93106
§*Department of Chemistry, University of Southern California, Los Angeles, CA 90089*
∥*Department of Materials, University of Oxford, Parks Rd, Oxford OX1 3PH, UK*

E-mail: mbutala@umail.ucsb.edu; seshadri@mrl.ucsb.edu

1

Abstract

Complex manganese oxides have been extensively studied as intercalation Li-ion battery electrodes. The simple oxide MnO has been proposed as a conversion anode material with a theoretical capacity of $756\,\mathrm{mAh\,g^{-1}}$ for full reduction to the metal. We report the reaction of MnO with Li using in situ X-ray diffraction and find no sign of crystalline products upon either discharge or charge. However, the absence of reflections, paired with electrochemical impedance spectroscopy, suggests disordered discharge products. We also examine composite electrodes with porous particles of MnO as the active component, with pores generated through the reductive heating of Mn_3O_4. We compare the behavior of these with more dense MnO powders, including studies of the electrode morphologies pre- and post-cyling. We find differences in the first discharge relevant to the utility of such mesostructuring in conversion reaction materials. Specifically, we find this type of mesostructure, which gives advantage in intercalation and pseudocapacitive storage, does not yield the same benefits for conversion reaction systems.
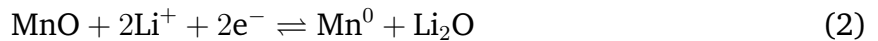
Introduction

The realization of Li-ion battery (LIB) technology that came with layered transition metal oxides is a key contributor to the ubiquitous nature of portable electronics. LIBs have more recently found use in electric vehicles. While the layered or channeled structures of intercalation-based LIBs outperform previous technologies, especially nickel-metal hydride and lead acid, there are fundamental limits to the achievable gravimetric capacities of intercalation materials, which are typically only $150\,\mathrm{mAh\,g^{-1}}$ to $250\,\mathrm{mAh\,g^{-1}}$.[1,2]

Given the perpetual drive for electrochemical energy storage with higher energy densities needed for lighter, smaller batteries, the number of studies on conversion electrode materials with theoretical capacities between $600\,\mathrm{mAh\,g^{-1}}$ and $1000\,\mathrm{mAh\,g^{-1}}$ has increased dramatically.[3] Initially considered to be feasible only at high temperatures with molten salt electrolytes,[4,5] transition metal oxides that store charge by conversion were found to exhibit reversibility at room temperature with sufficiently small particle sizes.[6] Since this revelation, a number of studies have reported the performance of M_aX_b compounds that react with Li by conversion, such that M = a transition metal and X = O, S, N, P, and F.[3,6] Conversion reactions are understood to follow as (Eq. 1):[6]

$$M_aX_b + (bn)\mathrm{Li}^+ + (bn)\mathrm{e}^- \rightleftharpoons aM^0 + b\mathrm{Li}_nX \tag{1}$$
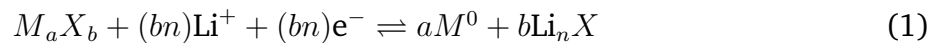
The application of Eq. 1 to MnO is (Eq. 2):

$$\mathrm{MnO} + 2\mathrm{Li}^+ + 2\mathrm{e}^- \rightleftharpoons \mathrm{Mn}^0 + \mathrm{Li}_2\mathrm{O} \tag{2}$$

A major issue that plagues conversion electrodes is significant irreversibility, which leads to poor coulombic efficiency and short cycle life. This is due in part to kinetic issues, though theoretical and experimental works have also found evidence of significant thermodynamic barriers to reversibility in displacement and conversion systems.[7–9] In addition to

3

chemical irreversibility, conversion materials undergo nanostructuring during the first discharge, whereupon initially micron or sub-micron particles are converted to nanoparticles of M^0 that are 2 nm to 5 nm in diameter in a matrix of disordered Li_nX.[10]

This study focuses on porous transition metal compounds, which have been extensively studied for surface-based energy storage, especially pseudocapacitors. Mesopores have been used to improve performance in several intercalation systems and are shown to have superior performance to nanoparticles.[11,12] Porosity has also been applied to transition metal oxide conversion materials in attempts to improve electrochemical performance, with hopes for porosity to deliver similar benefits to coulombic and energy efficiency as have been observed for intercalation and capacitive storage.[13–17]

We find here that porosity can yield temporary capacity improvement, but does not resolve the significant hysteresis and irreversibility encountered in conversion systems. Additionally, studies reporting on porous materials for conversion reactions only rarely detail why there are or are not advantages afforded by porosity, for example, by characterizing the morphology of the material with cycling, as we do here.[13,15,18,19]

Most reports of porous transition metal oxides for Li-ion batteries with charge storage by either intercalation or conversion have exclusively been prepared by templating. Here, we prepare porous MnO through spontaneous, template free routes, by heating dense Mn_3O_4 in a reducing atmosphere, based on methods reported by Toberer *et. al.*[20] We compare the benefits of mesopores on the order of 15 nm to 40 nm to nonporous MnO by galvanostatic cycling and investigate mesostructures before and after cycling by scanning electron microscopy (SEM). Additionally, we report in situ X-ray diffraction (XRD) and electrochemical impedance spectroscopy (EIS) for the conversion reaction of MnO with Li.

Experimental

Cell Assembly and Electrochemical Analysis

For in situ studies, as-purchased MnO powder (Alfa Aesar) and the conductive carbon additive SuperP® (TIMCAL) were ground by hand using an agate mortar and pestle in a 75:15 ratio by weight. The powders were dried overnight in a vacuum oven at 120 °C. In an Ar-filled glovebox, the loose powder cathode and Li metal anode were assembled into a cell with a Be window at the cathode side, which allowed the collection of XRD data in situ.[21] A glass fiber filter paper (Whatman® GF/D) separator prevented electrical shorting between electrodes. The electrolyte was a 1 M solution of lithium hexafluorophosphate (LiPF$_6$) in ethylene carbonate and diethyl carbonate (EC:DEC) in a 1:1 ratio by volume. In situ XRD data was collected on a Bruker D8 powder diffractometer with Co Kα ($\lambda =$ 1.79 Å) equipped with a LynxEye detector. Due to the cell configuration, data collection was limited to a 2θ range of 40° to 60°. Relevant reflections were primarily in the 40° to 50° range, so this region is the focus of in situ XRD analysis.

Electrochemical cycling was carried out using half-cells assembled in stainless steel 2032 coin cell cases (MTI). For coin cells, electrodes were a cast composite of MnO (either porous or nonporous), SuperP®, and polyvinylidene fluoride (PVDF) binder in a 75:10:15 ratio by weight. The electrode components were made into a slurry with N-methyl-2-pyrrolidone (NMP). The slurry was cast onto Cu foil using the Dr. Blade method and the cast film was dried on a hot plate at 120 °C for 3 hours. From the cast film, 15 mm diameter circles were cut out and dried in a vacuum oven at 120 °C overnight. The separator was a 19 mm diameter polypropylene sheet (Celgard). The electrolyte used was 1 M LiPF$_6$ in ethylene carbonate and dimethyl carbonate (EC:DMC) in a 1:1 ratio by volume. The reference electrode was 15 mm diameter scraped Li metal (STREM Chemicals). Cells were assembled in an Ar-filled glovebox.

Electrochemical measurements for in situ and cycling studies were performed using a

Bio-Logic VMP-3. Galvanostatic cycling with potential limitation (GCPL) was carried out at a rate of $C/20$, as calculated for the $2\,e^-$ reaction of MnO with 2 moles of Li, with an upper potential limit of 3 V and a lower potential limit of either 0.2 V or 0.01 V. For all cycling, rates and capacities were normalized to the mass of MnO in the electrode. During in situ GCPL, electrochemical impedance spectroscopy (EIS) data was collected in the frequency range of 500 kHz to 100 mHz at various states of charge. Data was collected with 6 points per decade and in logarithmic spacing, with a sinus amplitude of 10 mV and a waiting period of 0.10 s between each frequency.

Preparation of Porous MnO

Porous MnO was prepared as reported by Toberer *et. al.*[20] MnO powder was ground and pressed into 13 mm pellets using 5 metric tons of force. Pellets were sintered at 950 °C for 24 h and then quenched in water to retain Mn_3O_4, suppressing transformation to the room temperature equilibrium phase, Mn_2O_3. Mn_3O_4 was reduced to MnO at 475°C for 6 h in flowing 5% H_2 in N_2 gas.[20] X-ray diffraction (XRD), using a Philips X'Pert Diffractometer with Cu Kα radiation ($\lambda = 1.5418\,\text{Å}$) in the 2θ range of 10° to 100°, and Rietveld refinement, using Topas software,[22] confirmed the phase purity of the quenched and reduced products. Reduction to MnO involved a mass loss of about 6.9%, which was accommodated by the generation of connected pores on the order of 15 nm to 40 nm, as previously reported,[20] with pore walls of a similar size. The morphology of Mn_3O_4 and the resulting MnO were compared by SEM using an FEI XL40 Sirion FEG microscope. SEM samples were mounted with Cu tape and sputter-coated with Au/Pd to improve resolution and prevent charging. Images were collected with a beam voltage of 5 kV and a spot size of 3.

Results and Discussion

In situ XRD and Electrochemical Impedance Study of MnO Conversion

We carried out in situ XRD and EIS at several states of charge to learn about the conversion reaction of MnO with Li. For this experiment, the working electrode was nonporous MnO and SuperP® in a 75:15 ratio by weight against a Li metal anode using $1\,M$ $LiPF_6$ in EC:DEC electrolyte. The loose powder cell was cycled galvanostatically at a rate of $C/20$, calculated based on the reaction of MnO with 2 moles of Li (Eq. 2).[6]

The first cycle is shown in Figure 1(a), with time for the discharge on the lower x-axis and the corresponding capacity on the upper x-axis. XRD collected during the first discharge is shown in Figure 1(b) as a function of time, which is aligned with the time axis of the GCPL in Figure 1(a). Figure 1(c) shows select XRD patterns, which provide visualization of the relative intensity of MnO reflections before ($t = 0$), part way through ($t = 10$), and at the end of ($t = 24$) the first discharge. Before discharge ($t = 0$), there were intense MnO reflections at 41.0° and 47.5° in Co Kα 2θ and other, lower intensity peaks (marked with *) corresponding to Be and BeO from the window of the in situ cell.

There was a decrease in the intensity of MnO peaks during discharge, indicating the reaction of MnO with Li (Figure 1). However, XRD shows no crystalline discharge products. The proposed products from the reaction of MnO with 2 moles of Li are Mn^0 and Li_2O (Eq. 2).[6] We saw no crystalline Li_2O by XRD, due in part to the low Z elements of Li_2O which make it a weak X-ray scatterer. Also, Li_2O formed by conversion of a transition metal oxide is expected to have little-to-no long-range order, which limits phase identification of cycling products by XRD.[3,26] There are reports of crystalline Li_2O at the end of discharge, detected by ex situ XRD, with conversion of MnO and several higher valent Mn oxides.[27] However, various in situ studies see no evidence of crystalline Li_2O at the end of discharge, such as in the conversion of Mn_3O_4 and CoO.[6,26] These in situ results are in agreement with our findings, suggesting electrochemical products are amorphous, but
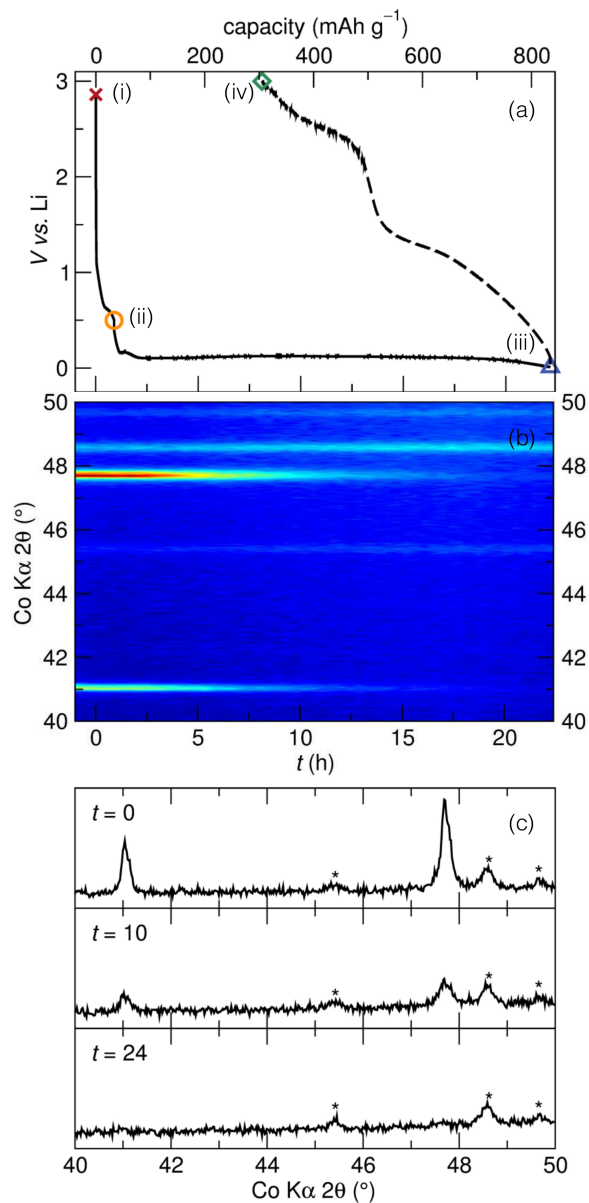
Figure 1: (a) GCPL at $C/20$ with potential limits of $0.01\,\mathrm{V}$ and $3\,\mathrm{V}$ was recorded for non-porous MnO, with EIS measured at various states of charge [(i), (ii), (iii), and (iv)] (EIS is shown in Figure 3). (b) In situ XRD for the first discharge is shown as a contour plot *vs.* discharge time. (b) Initial MnO reflections at $41.0°$ and $47.5°$ in Co Kα 2θ do not change concurrent with a small plateau near $0.6\,\mathrm{V}$ (a). (b) Along the discharge plateau, MnO peaks decrease in intensity until disappearing at end of discharge. XRD on charge is not shown, but MnO peaks do not return between the end of discharge and end of charge, and no new peaks evolve. (c) Select XRD scans are shown, with * for peaks associated with Be or BeO from the window of the in situ cell.
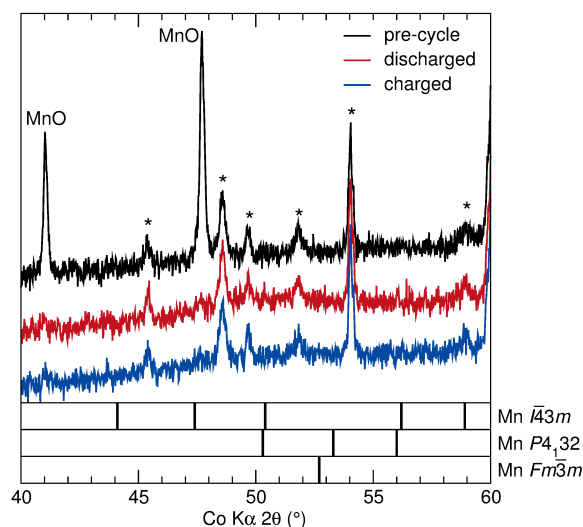
8

Figure 2: XRD collected before cycling shows two MnO reflections, which decreased in intensity during discharge. No other peaks formed with either discharge or charge. The sets of vertical lines at the bottom of the figure indicate the expected peak positions of various crystalline Mn^0 phases that could form. Data for these phases are plotted from ICSD entries 42743,[23] 41775,[24] and 41509.[25] MnO peaks do not return with charge, which is suggestive of a charge product with no long-range order.

have the opportunity to crystallize during ex situ experiments.

Several phases of Mn^0 could form on discharge, but none of which were observed (Figure 2). However, disordered Mn^0 could account for the lack of reflections at the end of discharge. Additionally, if there were broad, low intensity peaks coming from 2 nm to 5 nm particles,[26] the signal could be lower than the background of the XRD data. Jiao *et. al* also found no evidence of crystalline Mn^0 at the end of discharge for Mn_3O_4 by XRD, but did see locally ordered Mn^0 by X-ray absorption spectroscopy.[26]

Furthermore, we do not see evidence for the reformation of crystalline MnO on charge (Figure 2). This is in agreement with similar in situ studies of transition metal oxide conversion electrode materials, especially CoO.[6] Our findings are also consistent with those of the in operando characterization of Mn_3O_4, in which charge product(s) showed no crystalline phase by XRD, but locally resembled MnO.[26] Ex situ X-ray absorption near edge spectroscopy (XANES) of MnO conversion saw some, but not complete, oxidation of Mn to the 2+ state upon charge.[28] Charge products with only local, rather than long range,

9

order have also been observed for MnO and NiO, among others.[9,28,29]
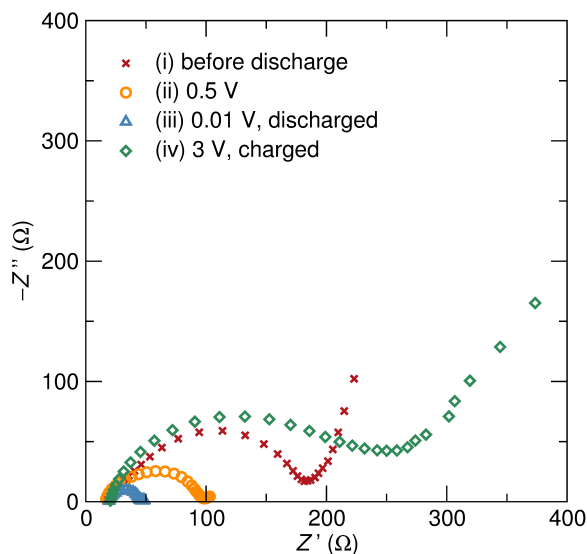

Figure 3: EIS was recorded at various states of charge during galvanostatic cycling, which are marked in Figure 1(a). The spectra are shown here in a Nyquist plot. (i) The impedance before discharge was moderate and (ii) decreased with discharge to 0.5 V. (iii) Impedance decreased further with complete discharge to 0.01 V. (iv) With charge to 3 V, both the imaginary and real components of impedance increased.

While in situ XRD provides only partial phase information for the cycling of MnO, namely the conversion of MnO to X-ray amorphous product(s) upon discharge and charge, we can gain insight about the nature of the products from EIS recorded at various states of charge, marked in the GCPL in Figure 1(a) as (i), (ii), (iii), and (iv). The collected spectra are shown in Figure 3 by the same labels. Before discharge (i), the loose powder cathode has an impedance spectra with a semicircle at low impedance and a tail at higher impedances. With discharge to 0.5 V (ii), just beyond the small plateau in GCPL, the size of the upper intercept of the semicircle is decreased, suggesting a decrease in charge transfer resistance. By XRD, we see no change in the MnO peak intensities at this state of charge, so the small plateau [Figure 1(a)(ii)] and change in impedance likely result from solid electrolyte interphase (SEI) formation. SEI has been shown to occur near this potential for carbonate electrolytes and to reduce the charge transfer resistance.[30,31]

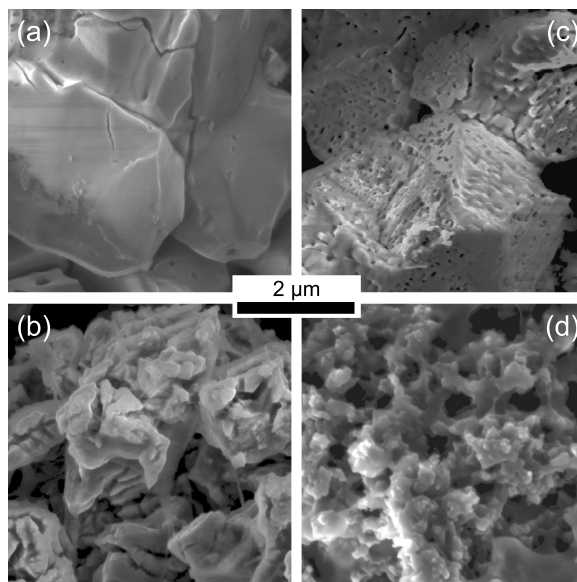At the end of discharge (iii), both the real and imaginary components of impedance

Figure 4: SEM of cast composites electrode of (a) nonporous MnO before cycling shows micron-sized grains. (b) The micrograph of nonporous MnO after cycling shows cracks and sub-micron features. (c) Porous MnO before cycling has 15 nm to 40 nm pores and pore walls. (d) The micrograph of cycled porous MnO shows that the pores have been destroyed and the dominant feature sizes resemble those of (b) nonporous MnO after cycling.

were again decreased. According to the model for conversion reactions, we expect Mn^0 nanoparticles in a matrix of disordered Li_2O at the end of discharge.[10,32] The decreased size of the semicircle could correspond to improved Li^+ conductivity, which suggests the formation of disordered Li_2O. This fits with the absence of Li_2O reflections by in situ XRD. Studies on FeF_2 conversion report a percolative network of Fe^0 nanoparticles upon discharge, expected to provide an electron conduction pathway through the sub-micron domains of the initial phase.[32] For discharged MnO, we saw negligible change in the low impedance (high frequency) regime of EIS, suggesting no enhanced electron conductivity upon discharge.

After charging to 3 V (iv), the semicircle grew beyond its initial size. Additionally, the high impedance intercept of the semicircle was less well-defined than before cycling (i). This could be the result of reduced homogeneity of the electrode-electrolyte interface after charge (iv), possibly arising from a variety of domain sizes or an increased roughness at the electrode interface, as observed by SEM after 20 cycles [Figure 4(b)]. Alternatively, the nature of the observed impedance could arise from the presence of various phases upon

charge. Since less than 60% of the discharge capacity was recovered with charge, we did not expect a single-phase product. Each different surface or phase present could contribute a different semicircle, the combination of which would give rise to the disperse and ill-defined end of the semicircle at mid-range frequencies upon charge. Other possibilities include a contribution of SEI or electrolyte decomposition to charged state EIS. While electrolyte interactions play a large role in some of our observations and, generally, in electrochemical energy storage materials that operate below $1\,\text{V}$, we focus here on the inorganic aspects of MnO conversion.

The combination of in situ XRD and EIS at various states of charge suggests the formation of small domains of amorphous phases from micron-sized particles at the end of the first discharge that persist with charge. By XRD, we also saw no crystalline phases at discharge or charge. The formation of disordered Li_2O at discharge is supported by XRD and decreased impedance. XRD and EIS support SEI formation during the plateau near $0.6\,\text{V}$, because the impedance shows a decrease in charge transfer resistance, but MnO reflection intensities in XRD show no change before and after this electrochemical feature.

Comparing nonporous and Porous MnO

As described in the experimental section, MnO with connected porosity was prepared by reducing Mn_3O_4, following the procedures described by Toberer *et. al.*[33] The phase and morphology of Mn_3O_4 were assessed by XRD and SEM. XRD and Rietveld refinement showed good agreement to sintered and quenched Mn_3O_4 [Figure 5(a)] and reduction to MnO [Figure 5(b)]. SEM shows macroscale porosity for Mn_3O_4 [Figure 6(a)] and smaller, secondary pores $15\,\text{nm}$ to $40\,\text{nm}$ wide in the reduced MnO [Figure 6(b)]. The nanoscale pores of MnO were evident at pellet surfaces and cross-sections, showing porosity was throughout the micron-sized grains. BET surface area and BJH pore size distribution for MnO prepared by the methods employed here have been previously reported by Toberer *et al.* from N_2 sorption measurements,[20] reporting low surface areas between $1\,\text{m}^2\ \text{g}^{-1}$
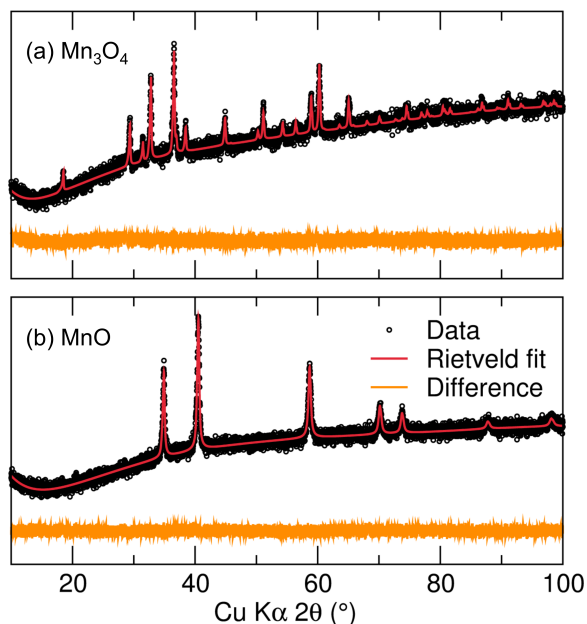
Figure 5: XRD and Rietveld refinement confirmed the phase purity of (a) Mn_3O_4 prepared by solid state methods and (b) reduction to MnO by heat treatment in flowing 5% H_2/N_2. XRD data is shown as black circles, the Rietveld fit is shown in red, and the difference is shown in orange.

and $6\,m^2\,g^{-1}$ with a pore size distribution centered at $50\,nm$.[20] We find similar pore size distributions by N_2 sorption measurements, consistent also with observations by SEM.

Based on previous studies,[6,34,35] we expected the smaller domain sizes and minor increase in surface area that accompany porosity to improve the capacity and capacity retention of the conversion reaction of MnO. We compared the electrochemical performance of micron-sized grains of MnO [Figure 4(a)] and MnO prepared by the reduction of Mn_3O_4 [Figure 4(c)]. Following, these will be referred to as nonporous and porous MnO, respectively.

Composite electrodes of nonporous and porous MnO were prepared with SuperP® and PVDF and cast onto Cu foil. Electrodes were tested in coin cells with $1\,M$ $LiPF_6$ in EC:DMC electrolyte against a Li metal anode. Galvanostatic cycling was carried out at $C/20$, calculated based on the reaction of MnO with 2 moles of Li (Eq. 2).[6]

The theoretical potential for the reaction of MnO with Li is $1.032\,V$ *vs.* Li/Li$^+$.[36] We carried out GCPL with an upper potential limit of $3\,V$ and a lower potential limit of either $0.2\,V$
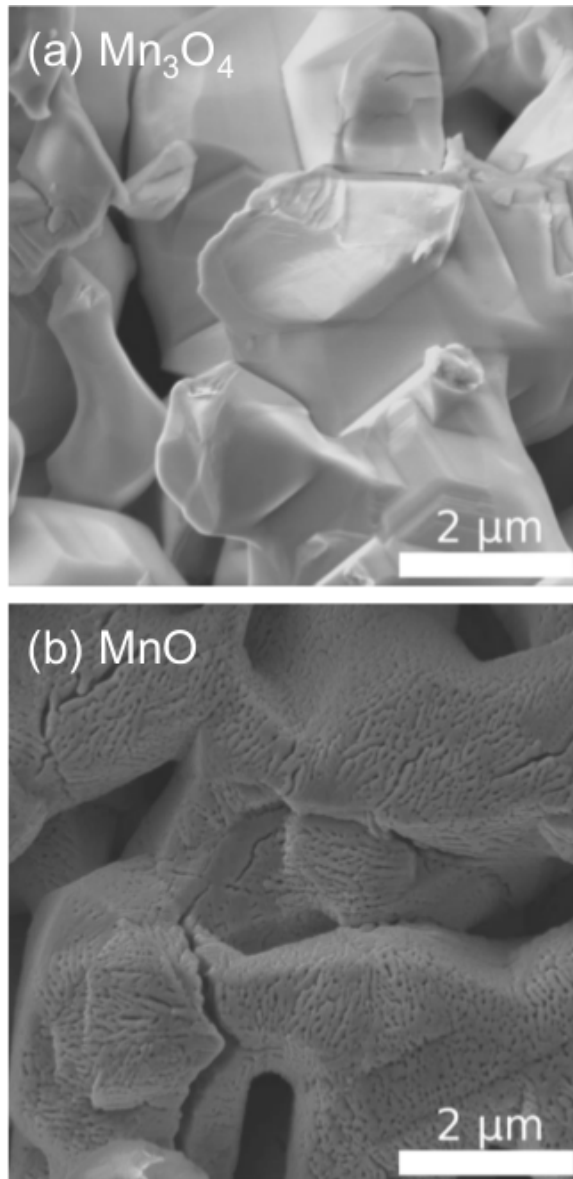
13

Figure 6: SEM of (a) Mn_3O_4 prepared by solid state methods showed micron-sized grains. (b) SEM after heating in flowing 5% H_2/N_2 shows pores and pore walls 15 nm and 40 nm wide throughout micron-sized grains.
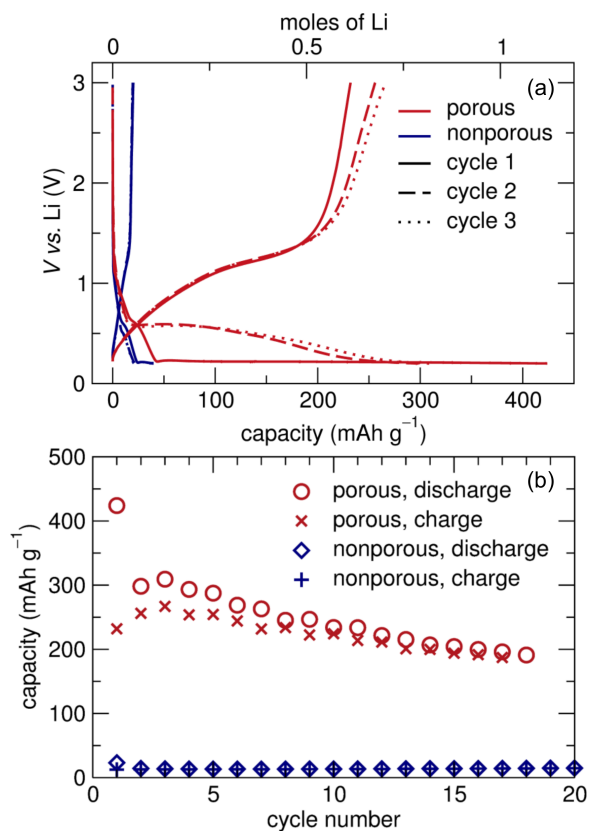
Figure 7: (a) The first three cycles of GCPL are shown for porous and nonporous MnO cycled at $C/20$ between 0.2 V and 3 V. The first cycle is shown with solid lines, the second with dashed lines, and the third with dotted lines. GCPL shows a large overpotential on the first discharge for porous and nonporous MnO. (b) Capacity per cycle is shown for porous and nonporous MnO, with discharge capacity shown by open shapes and charge capacity shown by closed shapes. With these potential limits, porous MnO appears to cycle better than nonporous MnO. However, (a) GCPL shows that neither cell achieved full discharge with this lower potential limit.

or 0.01 V. The first three cycles of GCPL with a lower potential limit of 0.2 V are shown in Figure 7(a) for porous and nonporous MnO and capacity per cycle is shown in Figure 7(b). For the discharge-charge profiles shown, electrodes had loadings of 5.6 mg cm^{-2} and 7.7 mg cm^{-2} of porous and nonporous MnO, respectively.

GCPL revealed a difference in the reaction potentials for porous and nonporous MnO on the first discharge. For both porous and nonporous MnO, there was a short plateau near 0.6 V associated with SEI formation, based on observations for nonporous MnO by in situ XRD and EIS and previous studies.[30,31] Beyond this short plateau, only negligible capacity was achieved for nonporous MnO over a short plateau at 0.2 V. Porous MnO also had a plateau near 0.2 V, but with an order of magnitude higher capacity.

In the second and third discharges of porous MnO, two plateaus were present, one sloping from 0.5 V to 0.25 V and a second near 0.2 V that resembled the first cycle discharge plateau. While two plateaus typically indicate two distinct chemical processes, for porous MnO the difference in potential of the two plateaus arises from microstructural, rather than chemical, differences in the processes taking place. Conversion electrodes have large overpotentials on the first discharge that result from the energy associated with nanostructural evolution from initial particles to nanoscale domains of discharge products.[6] Since the theoretical capacity was not achieved on the first discharge and the plateau did not end before the lower potential limit was reached, during the second discharge (1) the sloping plateau at 0.5 V comes from the reduction of active material that has already undergone reaction with Li in the first cycle and (2) the plateau at 0.2 V is the reaction of previously unreacted MnO with Li, with the same overpotential as the first discharge.

Nonporous MnO had negligible capacity in the first three cycles, with only a small fraction of the active material reacting with Li. Galvanostatic cycling and capacity per cycle number [Figure 7(a) and (b)] with a lower potential limit of 0.2 V suggest that porous MnO offers an advantage over nonporous MnO, with first discharge capacities of 425 mAh g^{-1} and 25 mAh g^{-1} and capacities near 200 mAh g^{-1} and 25 mAh g^{-1} approaching 20 cycles,
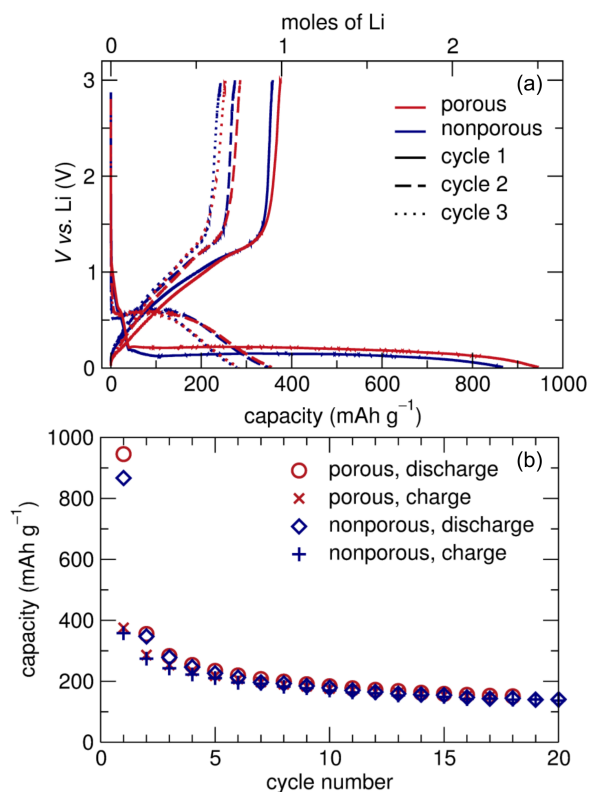
16

respectively.

Figure 8: (a) The first three cycles of GCPL are shown for porous and nonporous MnO cycled at $C/20$ between 0.01 V and 3 V. The first cycle is shown with solid lines, the second with dashed lines, and the third with dotted lines. For porous and nonporous MnO, there is a larger overpotential on the first discharge than in subsequent discharges. There is also irreversible capacity for both porous and nonporous MnO. (b) Gravimetric capacity per cycle is shown for porous and nonporous MnO. Discharge capacity is shown with open shapes and charge capacity is shown with closed shapes.

The cycling of porous and nonporous MnO with a lower potential limit of 0.01 V (Figure 8) shed light on the differences observed between porous and nonporous MnO cycled with a lower potential limit of 0.2 V (Figure 7). With a lower potential limit of 0.01 V, the cycling and capacity per cycle of porous and nonporous MnO were strikingly similar [Figure 8(a) and (b)]. For the discharge-charge profiles shown, electrodes had loadings of $6.0 \, \text{mg cm}^{-2}$ and $10.7 \, \text{mg cm}^{-2}$ of porous and nonporous MnO, respectively. Porous MnO had a first discharge capacity of $945 \, \text{mAh g}^{-1}$ and that of nonporous MnO was $865 \, \text{mAh g}^{-1}$. The first charge capacities for porous and nonporous MnO were also similar,

at $375\,\text{mAh}\,\text{g}^{-1}$ and $360\,\text{mAh}\,\text{g}^{-1}$, respectively. About 40% of the capacity was lost with the first charge, similar to that observed for porous MnO with a lower potential limit of 0.2 V (Figure 7).

A feature observed for porous and nonporous MnO regardless of lower potential limit was a small plateau near 0.6 V during discharge, just as was seen for in situ XRD of nonporous MnO [Figure 1(b)]. This feature is consistent with SEI formation.[30,31] On the first discharge with a lower potential limit of 0.01 V, the theoretical capacity of MnO ($756\,\text{mAh}\,\text{g}^{-1}$) was exceeded for both porous and nonporous MnO. The 0.6 V plateau in the first discharge contributes $25\,\text{mAh}\,\text{g}^{-1}$ and $50\,\text{mAh}\,\text{g}^{-1}$ for nonporous and porous MnO. Even taking this into account, the observed capacity exceeds the theoretical. Additional capacity may come from either storage by the conductive carbon additive or other electrolyte decomposition processes at low potentials.[9,30] The contribution of SEI to capacity and its influence on other aspects of cycling appear to be significant in transition metal oxides operating below 1 V and especially in those that are mesoporous, with more surface area upon which SEI can form.[13,15] Although EIS experiments showed a decrease in charge-transfer resistance following SEI formation (Figure 1 and Figure 3), the stability of the SEI with cycling was unclear.

With a lower potential limit of 0.01 V, there was a difference in the potential of the first discharge plateau for porous and nonporous MnO [Figure 8(a)]. The first discharge plateau began at 0.22 V for porous MnO and at 0.15 V for nonporous MnO [Figure 8(a)]. This explains the negligible capacity observed for nonporous MnO with a lower potential limit of 0.2 V. As mentioned, a higher overpotential is typically observed for the first discharge of conversion materials. The apparent benefit of mesopores to capacity for MnO cycled with a lower potential limit of 0.2 V is simply an exaggerated manifestation of the decreased first discharge overpotential of porous MnO relative to nonporous MnO (Figure 7). Ponrouch *et. al* saw a similar difference in overpotential with temperature between NiO cycled at room temperature and at 150°C.[37] For NiO, the temperature had a similar

effect to that observed here between nonporous and porous MnO.

However, the difference in the first discharge overpotential does not explain the similar performance for porous and nonporous MnO after the first cycle with a lower potential limit of 0.01 V. Rather, by GCPL (Figure 8) any benefit of porosity was lost beyond the first discharge. SEM of MnO electrodes pre- and post-cycling showed significant microstructural changes for both nonporous and porous MnO after 20 cycles (Figure 4). In Figure 4(a) and (c), we see initial domain sizes on the order of microns for nonporous MnO and tens of nanometers for porous MnO. SEM showed that initially distinct porous and nonporous MnO closely resembled one another after cycling; the micron-sized grains of nonporous MnO were broken down into smaller domains and the small pores of porous MnO were destroyed with repeated volume expansion and contraction during cycling.

Similar observations have been made for the conversion reaction of Co_3O_4 with 10 nm pores (generated through templating) by two groups via ex situ TEM and small angle X-ray scattering.[13,18] These results of destroyed mesopores in the first few cycles are in contrast to those of Dupont *et. al* for mesoporous Cr_2O_3, for which porosity persisted through at least 40 cycles.[15] Regardless of how long the structures lasted with cycling, for each mesoporous system the capacity with cycling resembled that of its nonporous, micron-sized analogue upon loss of porosity.[13,15,18] Mesoporous Cr_2O_3 also had a decreased overpotential relative to the bulk initially, but beyond the first cycle had the same hysteresis as bulk Cr_2O_3.[15]

Conclusions

We find the electrochemical conversion reaction of MnO with Li to form X-ray amorphous products. This is evidenced by the decreasing intensity of MnO reflections over the first discharge and the absence of any emerging peaks by in situ XRD. EIS suggests SEI formation at 0.6 V and discharge products with lower impedance than the initial phase. These observations support that presence of disordered, rather than crystalline, discharge prod-

ucts that locally resemble Mn^0 and Li_2O. Charge products also appear amorphous, and less than 60% of the first discharge capacity was recovered upon charge. We are unable to determine the chemistry of the charge product(s) by XRD, but expect that they locally resemble MnO.[9,26]

We observe a higher capacity and lower overpotential on the first discharge for porous relative to nonporous MnO. In the appropriate potential range, we find strikingly similar cycling for nonporous and porous MnO. SEM reveals significant mesoscale changes with cycling, including the destruction of mesopores. While it is known that conversion electrodes undergo extensive changes at the atomic and nanoscale, we find the nature of conversion also impacts the mesoscale. Accordingly, mesoscale structures, such as porosity, do not yield the same lasting benefits to conversion materials as as they afford in intercalation and pseudocapacitor electrode materials.

Acknowledgements

References

(1) Hayner, C. M.; Zhao, X.; Kung, H. H. Materials for Rechargeable Lithium-Ion Batteries. *Annu. Rev. Chem. Biomol. Eng.* **2012**, *3*, 445–471.

(2) Melot, B. C.; Tarascon, J. M. Design and Preparation of Materials for Advanced Electrochemical Storage. *Acc. Chem. Res.* **2013**, *46*, 1226–1238.

(3) Cabana, J.; Monconduit, L.; Larcher, D.; Palacín, M. R. Beyond Intercalation-Based Li-Ion Batteries: The State of the Art and Challenges of Electrode Materials Reacting Through Conversion Reactions. *Adv. Mater.* **2010**, *22*, E170–E192.

(4) Godshall, N. A.; Raistrick, I. D.; Huggins, R. A. Thermodynamic Investigations of Ternary Lithium-Transition Metal-Oxygen Cathode Materials. *Mater. Res. Bull.* **1980**, *15*, 561–570.

(5) Thackeray, M. M.; Coetzer, J. A Preliminary Investigation of the Electrochemical Performance of α-Fe$_2$O$_3$ and Fe$_3$O$_4$ Cathodes in High-Temperature Cells. *Mater. Res. Bull.* **1981**, *16*, 591–597.

(6) Poizot, P.; Laruelle, S.; Grugeon, S.; Dupont, L.; Tarascon, J. M. Nano-Sized Transition-Metal Oxides as Negative-Electrode Materials for Lithium-Ion Batteries. *Nature* **2000**, *407*, 496–499.

(7) Yu, H.-C.; Ling, C.; Bhattacharya, J.; Thomas, J. C.; Thornton, K.; Van der Ven, A. Designing the Next Generation of High Capacity Battery Electrodes. *Energy Environ. Sci.* **2014**, *7*, 1760–1768.

(8) Mestre-Aizpurua, F.; Laruelle, S.; Grugeon, S.; Tarascon, J. M.; Palacín, M. R. High Temperature Lithium Cells Using Conversion Oxide Electrodes. *J. Appl. Electrochem.* **2010**, *40*, 1365–1370.

(9) Boesenberg, U.; Marcus, M. A.; Shukla, A. K.; Yi, T.; McDermott, E.; Teh, P. F.; Srinivasan, M.; Moewes, A.; Cabana, J. Asymmetric Pathways in the Electrochemical Conversion Reaction of NiO as Battery Electrode with High Storage Capacity. *Sci. Rep.* **2014**, *4*, 7133:1–7133:9.

(10) Wang, F.; Yu, H.; Chen, M.; Wu, L.; Pereira, N.; Thornton, K.; Van der Ven, A.; Zhu, Y.; Amatucci, G. G.; Graetz, J. Tracking Lithium Transport and Electrochemical Reactions in Nanoparticles. *Nat. Commun.* **2012**, *3*, 1201–1208.

(11) Jiao, F.; Bao, J.; Hill, A. H.; Bruce, P. G. Synthesis of Ordered Mesoporous Li−Mn−O Spinel as a Positive Electrode for Rechargeable Lithium Batteries. *Angew. Chem.* **2008**, *120,* 9857–9862.

(12) Ren, Y.; Armstrong, A. R.; Jiao, F.; Bruce, P. G. Influence of Size on the Rate of Mesoporous Electrodes for Lithium Batteries. *J. Am. Chem. Soc.* **2010**, *132*, 966–1004.

(13) Shaju, K. M.; Jiao, F.; Débart, A.; Bruce, P. G. Mesoporous and Nanowire Co_3O_4 as Negative Electrodes for Rechargeable Lithium Batteries. *Phys. Chem. Chem. Phys.* **2007**, *9*, 1837–1842.

(14) Jiao, F.; Bao, J.; Bruce, P. G. Factors Influencing the Rate of Fe_2O_3 Conversion Reaction. *Electrochem. Solid-State Lett.* **2007**, *10*, A264–A266.

(15) Dupont, L.; Laruelle, S.; Grugeon, S.; Dickinson, C.; Zhou, W.; Tarascon, J. M. Mesoporous Cr_2O_3 as Negative Electrode in Lithium Batteries: TEM Study of the Texture Effect on the Polymeric Layer Formation. *J. Power Sources* **2008**, *175*, 502–509.

(16) Shi, Y.; Guo, B.; Corr, S. A.; Shi, Q.; Hu, Y.-S.; Heier, K. R.; Chen, L.; Seshadri, R.; Stucky, G. D. Ordered Mesoporous Metallic MoO_2 Materials with Highly Reversible Lithium Storage Capacity. *Nano Lett.* **2009**, *9*, 4215–4220.

(17) Cao, Y.; Fang, D.; Liu, R.; Jiang, M.; Zhang, H.; Li, G.; Luo, Z.; Liu, X.; Xu, J.; Xu, W.; Xiong, C. Microwave-assisted Synthesis of Mesoporous Co_3O_4 Nanoflakes for Applications in Lithium Ion Batteries and Oxygen Evolution Reactions. *ACS Appl. Mater. Interfaces* **2015**, *7*, 27685–27693.

(18) Park, G. O.; Yoon, J.; Park, E.; Park, S. B.; Kim, H.; Kim, K. H.; Jin, X.; Shin, T. J.; Kim, H.; Yoon, W.-S.; Kim, J. M. *In Operando* Monitoring of the Pore Dynamics in Ordered Mesoporous Electrode Materials by Small Angle X-ray Scattering. *ACS Nano.* **2015**, *9*, 5470–5477.

(19) Li, K.; Shua, F.; Guo, X.; Xue, D. High Performance Porous MnO@C Composite Anode Materials for Lithium-Ion Batteries. *Electrochim. Acta* **2016**, *188*, 793–800.

(20) Toberer, E. S.; Schladt, T. D.; Seshadri, R. Macroporous Manganese Oxides with Regenerative Mesopores. *J. Am. Chem. Soc.* **2006**, *128*, 1462–1463.

(21) Morcrette, M.; Chabra, Y.; Vaughan, G.; Amatucci, G.; Leriche, J.-B.; Patoux, S.; Masquelier, C.; Tarascon, J. M. In Situ X-ray Diffraction Techniques as a Powerful Tool to Study Battery Electrode Materials. *Electrochim. Acta.* **2002**, *47*, 3137–3149.

(22) Coelho, A. Topas Academic V4.1. Coelho Software, Brisbane, Australia. **2007**,

(23) Oberteuffer, J. A.; Ibers, J. A. A Refinement of the Atomic and Thermal Parameters of α-Manganese from a Single Crystal. *Acta. Crystallogr., Sect. B: Struct. Sci.* **1970**, *26*, 1499–1504.

(24) Shoemaker, C. B.; Shoemaker, D. P.; Hopkins, T. E.; Yindepit, S. Refinement of the Structure of β-Manganese and of a Related Phase in the Mn–Ni–Si System. *Acta. Crystallogr., Sect. B: Struct. Sci.* **1978**, *34*, 3573–3576.

(25) Haglund, J.; Guillermet, F. F.; Grimvall, G.; Korling, M. Theory of Bonding in Transition-Metal Carbides and Nitrides. *Phys. Rev. B* **1993**, *48*, 11685–11691.

(26) Lowe, M. A.; Gao, J.; Abruña, H. D. In Operando X-ray Studies of the Conversion Reaction in Mn_3O_4 Lithium Battery Anodes. *J. Mater. Chem. A* **2013**, *1*, 2094–2103.

(27) Fang, X.; Lu, X.; Guo, X.; Mao, Y.; Hu, Y.-S.; Wang, J.; Wang, Z.; Wu, F.; Liu, H.; Chen, L. Electrode Reactions of Manganese Oxides for Secondary Lithium Batteries. *Electrochem. Commun.* **2010**, *123*, 1520–1523.

(28) Zhong, K.; Zhang, B.; Luo, S.; Wen, W.; Li, H.; Huang, X.; Chen, L. Investigation on Porous MnO Microsphere Anode for Lithium Ion Batteries. *J. Power Sources.* **2011**, *196*, 6802–6808.

(29) Hua, X.; Robert, R.; Du, L.-S.; Wiaderek, K. M.; Leskes, M.; Chapman, K. W.; Chupas, P. J.; Grey, C. P. Comprehensive Study of the CuF_2 Conversion Reaction Mechanism in a Lithium Ion Battery. *J. Phys. Chem. C* **2014**, *118*, 15169–15184.

(30) Balaya, P.; Bhattacharyya, A.; Jamnik, J.; Zhukovskii, Y.; Kotomin, E.; Maier, J. Nano-Ionics in the Context of Lithium Batteries. *J. Power Sources* **2006**, *159*, 171–178.

(31) Débart, A.; Dupont, L.; Poizot, P.; Leriche, J.-B.; Tarascon, J. M. A Transmission Electron Microscopy Study of the Reactivity Mechanism of Tailor-Made CuO Particles toward Lithium. *J. Electrochem. Soc.* **2001**, *148*, A1266–A1274.

(32) Wang, F.; Yu, H.-C.; Van der Ven, A.; Thornton, K.; Pereira, N.; Zhu, Y.; Amatucci, G. G.; Graetz, J. Ionic and Electronic Transport in Metal Fluoride Conversion Electrodes. *ECS Trans.* **2012**, *50*, 19–25.

(33) Toberer, E. S.; Grossman, M.; Schladt, T.; Lange, F. F.; Seshadri, R. Epitaxial Manganese Oxide Thin Films wth Connected Porosity: Topotactic Induction of Crystallographic Pore Alignment. *Chem. Mater.* **2007**, *19*, 4833–4838.

(34) Aricó, A. S.; Bruce, P.; Scrosati, B.; Tarascon, J. M.; Schalkwijk, W. V. Nanostructured

Materials for Advanced Energy Conversion and Storage Devices. *Nat. Mater.* **2005**, *4*, 366–377.

(35) Bruce, P.; Scrosati, B.; Tarascon, J. M. Nanomaterials for Rechargeable Lithium Batteries. *Angew. Chem. Int. Ed.* **2008**, *47*, 2930–2946.

(36) Li, H.; Balaya, P.; Maier, J. Li-Storage via Heterogeneous Reaction in Selected Binary Metal Fluorides and Oxides. *J. Electrochem. Soc.* **2004**, *151*, A1878–A1885.

(37) Ponrouch, A.; Cabana, J.; Dugas, R.; Slack, J. L.; Palacin, R. M. Electroanalytical Study of the Viability of Conversion Reactions as Energy Storage Mechanisms. *RSC Adv.* **2014**, *4*, 35988–35996.

Graphical TOC Entry